Distribution of radiative energy in ground fog

By GÜNTHER KORB, *Institut für Meteorologie, Universität Mainz*,

and

WILFORD ZDUNKOWSKI, *Department of Meteorology, University of Utah*

(Manuscript received May 5, 1969; revised version February 11, 1970)

ABSTRACT

This study deals with the distribution of solar and infrared radiation in a multiple scattering and absorbing fog consisting of water droplets and water vapor. An iterative solution of the radiative transfer equation, as formulated by Chandrasekhar (1960), is presented here, which is utilized to obtain radiative intensities, fluxes and their vertical divergence for the entire infrared spectrum. A sufficient number of sample computations is carried out also in the solar spectrum such as to verify the applicability of the numerical procedure for the entire heat spectrum. All calculations are made for two fog models, representing low and high fog for a liquid cloud water concentration of 0.1 g per cubic meter. The exact structure of spectral lines is taken into account. Computational results verify the applicability of the method for the entire spectrum for a fog extending to a height of at least 160 m. It is believed that the computational procedure as developed is capable also of obtaining information about the radiative behavior of clouds and fogs of far greater thickness.

1. Introduction

The prediction of radiation fog and its behavior after formation represents a very intriguing but also very difficult problem which presently has not been solved satisfactorily on a physical-mathematical basis. Two excellent studies on this subject are due to Kraus (1958) and Rodhe (1962). Both authors treat the radiation problem in a very simplified manner and, therefore, do not claim great accuracy in their radiation treatment. A newer study by Zdunkowski & Nielsen (1969) treats the radiation problem in a more exact manner by accounting for the overlap effect of water vapor and water droplets in addition to using exact Mie computations. Their study of the radiation problem is still incomplete in two respects: the influence of droplet scattering and the possible effects of solar radiation are still disregarded.

In order to treat the problem complex of the prediction and maintenance of radiation fog in an entirely satisfactory manner, the influence of radiation alone must be understood first. Effects of moisture diffusion and heat conduction can be added at a later time. It is the purpose of this paper to present an exact method permitting the computation of radiative fluxes and their divergences in the presence of gaseous and droplet absorption and emission as well as multiple scattering. By specifying the water droplet distribution function, as thought to apply to fog, numerous attenuation coefficients and scattering functions are computed and utilized in obtaining fluxes and radiative temperature changes for the entire infrared spectrum. Furthermore, sample computations for the solar spectrum are presented to demonstrate the applicability of the method for flux computations pertaining to the entire spectrum.

Two fog models are used in this study, a high fog extending to 160 m and a low fog extending to 160 cm. Due to the complicated nature of the scattering function which at times requires an expansion into a series of Legendre polynomials of 150 terms, it is not possible to include polarization effects.

Mathematically, the entire problem consists of solving the radiative transfer equation as formulated in an exact manner by Chandrasekhar (1960). His general formulation will be used to include explicitly the influence of particle and gaseous emission and absorption utilizing the exact mathematical formulation of a spectral line. No further reference will be made to Chandrasekhar.

2. Mathematical analysis

2.1. *Definitions*

In order to give a brief and coherent presentation of the basic equations, it is first necessary to define the most important quantities which arise in Section 2.

$I_\lambda(\tau_\lambda, \mu, \phi)$ radiative intensity at wave length λ, at optical depth τ_λ and directions μ, ϕ.

$\tau_\lambda = -\int_H^z(\beta_\lambda + K_\lambda)dz$ optical depth in terms of the droplet extinction coefficient β_λ and the absorption coefficient K_λ of atmospheric gases. z stands for the height and H represents the altitude of the upper fog boundary.

ϑ, ϕ zenith and azimuthal distances of the radiative intensity, with $\mu = \cos\vartheta$.

ϑ', ϕ' zenith and azimuthal distances of previously scattered light, with $\mu' = \cos\vartheta'$.

$-\mu_0$, ϕ_0 direction of the parallel solar radiation.

$J_\lambda(\tau_\lambda, \mu, \phi)$ source function.

$I_{1,\lambda}(\tau_\lambda, \mu, \phi) = I_\lambda(\tau_\lambda, +\mu, \phi)$ = upwardly directed radiative intensity.

$I_{2,\lambda}(\tau_\lambda, \mu, \phi) = I_\lambda(_\lambda, -\mu, \phi)$ = downwardly directed radiative intensity.

$J_{1,\lambda}(\tau_\lambda, \mu, \phi)$ source function for $I_{1,\lambda}(\tau_\lambda, \mu, \phi)$.

$J_{2,\lambda}(\tau_\lambda, \mu, \phi)$ source function for $I_{2,\lambda}(\tau_\lambda, \mu, \phi)$.

$E_{0,\lambda}$ intensity of solar radiation at the upper boundary of the fog.

E_R solar intensity at the top of the atmosphere.

B_λ Planckian emission function.

$B_{G,\lambda}$ black body radiation of the ground.

k_λ total absorption coefficient divided by total extinction coefficient. It is treated as a constant in this investigation.

$\delta_{0,m}$ $\begin{Bmatrix} 1, \text{ if } m=0 \\ 0, \text{ if } m \neq 0 \end{Bmatrix}$ = Kronecker symbol.

$p_\lambda(\cos\theta)$ phase function of water droplets. θ is the scattering angle. $p_\lambda(\cos\theta)$ must be normalized so that energy is conserved. This results in the condition:

$$\frac{1}{4\pi}\int p_\lambda(\cos\theta)\,d\omega' = 1 \qquad (1)$$

where the integration is to be extended over the unit sphere surrounding an elemental scattering volume.

In this investigation, the solution of the radiative transfer equation is based upon the expansion of the phase function into a series of Legendre polynomials, i.e.

$$p_\lambda(\cos\theta) = \sum_{l=0}^{N} p_{l,\lambda} P_l(\cos\theta) \qquad (2)$$

with P_l denoting the Legendre polynomials. The coefficients of the series $p_{l,\lambda}$ are to be determined from electromagnetic theory and by specifying a droplet distribution function. In terms of (μ, ϕ; μ', ϕ') and by introducing the associated Legendre functions P_l^m the expansion (2) can be written

$$p(\mu, \phi; \mu', \phi') = \sum_{m=0}^{N} (2-\delta_{0,m}) \times \left\{\sum_{l=m}^{N} p_{l,\lambda}^m P_l^m(\mu) P_l^m(\mu')\right\} \cos m(\phi'-\phi) \qquad (3)$$

where

$$p_{l,\lambda}^m = p_{l,\lambda}\frac{(l-m)!}{(l+m)!}; \quad \begin{matrix} l=m, \ldots, N \\ 0 \leq m \leq N \end{matrix}$$

In connection with the expansion of the phase function into a series of Legendre polynomials, the following symbols are introduced:

$$F_{1,\lambda}^{(m)}(\mu, \mu_0) = \sum_{l=m}^{N} (-1)^{l+m} p_{l,\lambda}^m P_l^m(\mu) P_l^m(\mu_0)$$

$$F_{2,\lambda}^{(m)}(\mu, \mu_0) = \sum_{l=m}^{N} p_{l,\lambda}^m P_l^m(\mu) P_l^m(\mu_0)$$

$$R_{1,\lambda}^{(m)}(\mu, \mu') = \sum_{l=m}^{N} p_{l,\lambda}^m P_l^m(\mu) P_l^m(\mu')$$

$$R_{2,\lambda}^{(m)}(\mu, \mu') = \sum_{l=m}^{N} (-1)^{l+m} p_{l,\lambda}^m P_l^m(\mu) P_l^m(\mu') \qquad (4)$$

For reasons of simplicity, the reference to wave length is omitted from now on.

2.2. *Solution of the radiative transfer equation*

It is assumed that the ground fog, whose lower boundary is the surface of the earth, can be described as a plane-parallel and infinitely far extended horizontal layer of finite optical thickness. This layer is illuminated from above by parallel solar radiation and the diffuse radiation of atmospheric gases. Scattering processes of solar light above the fog are disregarded. The entire extinction process of the sun's energy, before reaching the cloud top, is therefore due to absorption. This means that by far the largest part of the solar radiation is still parallel at the top of the fog. If the albedo of the ground is not taken into account, the fog is illuminated from below only by means of the black body radiation of the earth's surface.

Inside the fog layer, however, processes due to scattering and absorption are taking place in the presence of true emission of cloud droplets and atmospheric gases. Therefore, the diffuse radiation field existing inside the fog is described by Chandrasekhar's complete equation of radiative transfer.

The phase function, occurring in the radiative transfer equation, is expanded into a series of Legendre polynomials. This makes it possible to seek a solution of the transfer equation in the form

$$I(\tau,\mu,\phi) = \sum_{m=0}^{N} I^{(m)}(\tau,\mu)\cos m(\phi_0-\phi) \qquad (5)$$

This procedure results in the elimination of the azimuthal dependency of the transfer equation due to the orthogonality relations of the angular functions. The determination of the diffuse radiation field inside the fog layer and at its boundaries requires the solution of the radiative transfer equation. According to the fog model, as described above, the following boundary conditions are adopted:

Top of the fog layer:

$$\tau=0,\ I_2^{(m=0)}(\tau=0,\mu)\neq 0;\quad I_2^{(m\neq 0)}(\tau=0,\mu)=0$$

Surface of the earth (albedo = 0):

$$\tau=T,\ I_1^{(m=0)}(T,\mu)=B_G;\quad I_1^{(m\neq 0)}(T,\mu)=0 \qquad (6)$$

Inspection of equation (6) indicates that the diffuse radiation, incident at the upper fog boundary, is assumed to be independent of the azimuthal angle. The quantity $I_2^{(m=0)}(\tau=0,\mu)$ depends only on the temperature and moisture distribution of the atmosphere above the fog as well as on the carbon dioxide mixing ratio of the air. Therefore, $I_2^{(m=0)}(\tau=0,\mu)$ must be evaluated for each direction of incidence and for each wave length using the Lorentz formulation of the distribution of absorption along a spectral line. Furthermore, formula (6) does not include the parallel solar radiation which is accounted for by an additional term in the source function of the transfer equation.

With the above boundary conditions, the formal solution of the equation of radiative transfer is found to be

$$I_1^{(m)}(\tau,\mu)=I_1^{(m)}(T,\mu)\,e^{-(T-\tau)/\mu} + \int_\tau^T J_1^{(m)}(t,\mu)\,e^{-(t-\tau)/\mu}\frac{dt}{\mu}$$

$$I_2^{(m)}(\tau,\mu)=I_2^{(m)}(\tau=0,\mu)\,e^{-\tau/\mu} + \int_0^\tau J_2^{(m)}(t,\mu)\,e^{-(\tau-t)/\mu}\frac{dt}{\mu} \qquad (7)$$

The source functions are given by

$$J_1^{(m)}(t,\mu)=\frac{1-k}{2}\int_0^1\left[I_1^{(m)}(t,\mu')R_1^{(m)}(\mu,\mu') + I_2^{(m)}(t,\mu')R_2^{(m)}(\mu,\mu')\right]d\mu' + (1-k)(2-\delta_{0,m}) \times \frac{E_0}{4\pi}e^{-t/\mu_0}F_1^{(m)}(\mu,\mu_0)+\delta_{0,m}kB(t)$$

$$J_2^{(m)}(t,\mu)=\frac{1-k}{2}\int_0^1\left[I_1^{(m)}(t,\mu')R_2^{(m)}(\mu,\mu') + I_2^{(m)}(t,\mu')R_1^{(m)}(\mu,\mu')\right]d\mu' + (1-k)(2-\delta_{0,m}) \times \frac{E_0}{4\pi}e^{-t/\mu_0}F_2^{(m)}(\mu,\mu_0)+\delta_{0,m}kB(t) \qquad (8)$$

As will be recognized, the source functions consist of three terms. The first terms, containing the integral expressions, deal with the effect of multiple scattering of water droplets. The terms containing E_0 and B represent the primary scattering of solar radiation and the true emission of cloud droplets and atmospheric gases.

Next, those terms of the source function are integrated in equation (7) which deal with the primary scattering of the solar radiation. Denoting this part of the diffuse radiation field in the fog layer by $I_{1,0}^{(m)}$ and $I_{2,0}^{(m)}$, one obtains

$$I_{1,0}^{(m)}(\tau,\mu) = (1-k)\frac{E_0}{4\pi}(2-\delta_{0,m})\frac{F_1^{(m)}(\mu,\mu_0)\,\mu_0}{\mu_0+\mu}$$
$$\times\,[e^{-\tau/\mu_0} - e^{+\tau/\mu}\cdot e^{-(\mu+\mu_0/\mu\mu_0)\,T}]$$
$$I_{2,0}^{(m)}(\tau,\mu) = (1-k)\frac{E_0}{4\pi}(2-\delta_{0,m})\frac{F_2^{(m)}(\mu,\mu_0)\,\mu_0}{\mu_0-\mu}$$
$$\times\,[e^{-\tau/\mu_0} - e^{-\tau/\mu}] \tag{9}$$

for $\quad \tau = 0 \quad 1 \geqslant \mu > 0$

$\qquad \tau \neq 0 \quad 1 \geqslant \mu \geqslant 0$

Evaluation of equation (9) requires the consideration of certain special cases. These are listed in Appendix 1.

Finally, to obtain a more compact and readable notation of equation (7) with (8), several terms are combined. The inclusion of the boundary conditions, as stated by equation (6), leads to the following definitions:

$$K_1^{(m)}(\tau,\mu) = I_{1,0}^{(m)}(\tau,\mu) + \int_\tau^T \delta_{0,m}\,kB(t)\,e^{-(t-\tau)/\mu}\frac{dt}{\mu}$$
$$+\,\delta_{0,m}\,B_G\,e^{-(T-\tau)/\mu}$$
$$K_2^{(m)}(\tau,\mu) = I_{2,0}^{(m)}(\tau,\mu) + \int_0^\tau \delta_{0,m}\,kB(t)\,e^{-(\tau-t)/\mu}\frac{dt}{\mu}$$
$$+\,I_2^{(m)}(0,\mu)\,e^{-\tau/\mu} \tag{10}$$

The remaining terms of (7) and (8) implicitly include the intensities of the diffuse radiation. For this reason, the following symbols are introduced.

$$Q_1^{(m)}(\tau,\mu;I_1^{(m)},I_2^{(m)}) = \frac{(1-k)}{2\mu}\int_\tau^T e^{-(t-\tau)/\mu}\,dt$$
$$\times\int_0^1 [I_1^{(m)}(t,\mu')\,R_1^{(m)}(\mu,\mu')$$
$$+\,I_2^{(m)}(t,\mu')\,R_2^{(m)}(\mu,\mu')]\,d\mu'$$

$$Q_2^{(m)}(\tau,\mu;I_1^{(m)},I_2^{(m)}) = \frac{(1-k)}{2\mu}\int_0^\tau e^{-(\tau-t)/\mu}\,dt$$
$$\times\int_0^1 [I_1^{(m)}(t,\mu')\,R_2^{(m)}(\mu,\mu')$$
$$+\,I_2^{(m)}(t,\mu')\,R_1^{(m)}(\mu,\mu')]\,d\mu' \tag{11}$$

Using equations (10) and (11), the solution equations (7) are now written as

$$I_1^{(m)}(\tau,\mu) = K_1^{(m)}(\tau,\mu) + Q_1^{(m)}(\tau,\mu;I_1^{(m)},I_2^{(m)})$$
$$I_2^{(m)}(\tau,\mu) = K_2^{(m)}(\tau,\mu) + Q_2^{(m)}(\tau,\mu;I_1^{(m)},I_2^{(m)}) \tag{12}$$

This type of solution to the radiative transfer equation is suitable for an iterative determination of the radiative intensities in the fog. The iterative procedure is discussed in section (3.4). It must be kept in mind, however, that the solution equation (12) pertains to monochromatic radiation only. The integration over the spectrum is described in a later section.

2.3. *Radiative fluxes*

The radiative flux is defined by means of

$$F = \sum_{m=0}^{N}\int_{-1}^{+1}\int_0^{2\pi} I^{(m)}(\tau,\mu)\cos m(\phi_0-\phi)\,\mu\,d\phi\,d\mu \tag{13}$$

This equation simplifies to

$$F = \int_{-1}^{+1}\int_0^{2\pi} I^{(m=0)}(\tau,\mu)\,\mu\,d\phi\,d\mu$$
$$= 2\pi\int_0^1 I_1^{(m=0)}(\tau,\mu)\,\mu\,d\mu$$
$$-\,2\pi\int_0^1 I_2^{(m=0)}(\tau,\mu)\,\mu\,d\mu \tag{14}$$

This simplification is due to the fact that $I^{(m)}$ is no longer a function of ϕ and that the integration of cos m $(\phi_0-\phi)$ is taken over a complete cycle. For the flux divergence computations that are required in this study, only the case $m=0$ needs to be considered. No such simplification will result if the exact distribution of the radiative intensities is sought.

3. Computational methods

3.1. *General considerations*

The atmosphere is subdivided into two main layers, D and E, which label the air above and within the ground fog. All optical path lengths will be measured downwardly and are counted zero at the top of each main layer as shown in Fig. 1.

Furthermore, for computational purposes it is convenient to consider the functional relationship of the Planck function versus optical path length instead of using $B(T)$ directly where T, exceptionally, stands for temperature. Such treatment is permissible since any τ corresponds to a unique atmospheric temperature. It is necessary to subdivide the main layers D and E into a number of suitable sublayers denoted by the running numbers 1, 2, ... m^*, ... n^*. Planck's function at the upper and lower boundary of each sublayer are denoted by $B_0^{(m^*)}$ and $B_u^{(m^*)}$ respectively. An example of the plot of B versus τ is shown for the E-layer in Fig. 2. As will be noticed, a main layer is subdivided in such a manner that each sublayer may be described by a linear distribution of $B(\tau)$. The total path length of layer E is given by

$$T_E = \sum_{j=1}^{n^*} T_E^{(j)} \tag{15}$$

Using the sublayer notation described above, one finds for the inclination $B_{E,1}^{(m^*)}$ of the Planckian curve of the m^*th sublayer

$$B_{E,1}^{(m^*)} = \frac{B_{E,u}^{(m^*)} - B_{E,0}^{(m^*)}}{T_E^{(m^*)}} = \frac{B_{E,0}^{(m^*+1)} - B_{E,0}^{(m^*)}}{T_E^{(m^*)}} \tag{16}$$

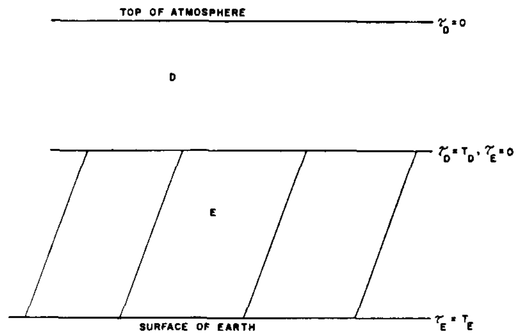

Fig. 1. Subdivision of the atmosphere.

The distribution of $B(\tau_E)$ in the m^*th layer is therefore given by

$$B_E^{(m^*)} = B_{E,0}^{(m^*)} + B_{E,1}^{(m^*)} \cdot \tau_E^{(m^*)} \tag{17}$$

where $\tau_E^{(m^*)}$ refers to any position within the m^*th sublayer.

3.2. *The computation of long wave radiative intensities outside the cloud*

In the troposphere the emission and absorption of infrared energy is almost exclusively due to water vapor and carbon dioxide. Atmospheric aerosols are disregarded. The radiative transfer by atmospheric gases is described by the Lorentz spectral line formula. The distribution of the absorption coefficient along such a line is given by

$$K_\lambda = \frac{K_{0,\lambda}(\alpha/2)^2}{(\lambda-\lambda_0)^2 + (\alpha/2)^2} \tag{18}$$

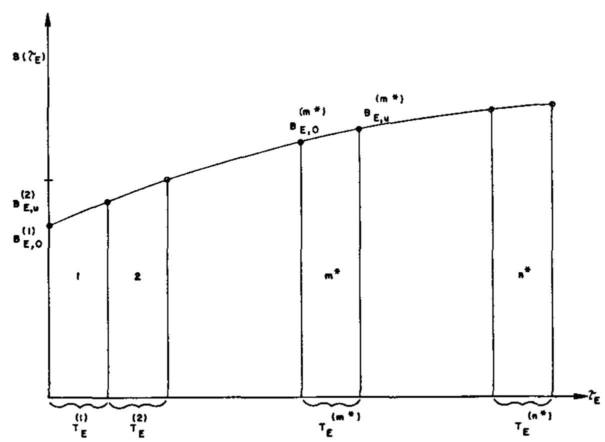

Fig. 2. Subdivision of the fog.

Here $K_{0,\lambda}$ is the value of the absorption coefficient at the center of the spectral line at $\lambda = \lambda_0$ and α is the half-width. Let $d \cdot \alpha$ define the distance over which a spectral line stretches itself. If ϱ_V stands for the density of the absorbing gas, p and p_0 for pressure and normal pressure, the average transmission $\mathbf{D}$ of the spectral line may be written in terms of the effective absorbing mass w, using the transformation variable $x = -(\lambda - \lambda_0)\,(\alpha/2)$ as

$$\mathbf{D}(w/\mu) = \frac{1}{d}\int_0^d \exp\left(-\frac{k_0\,\mu^{-1}}{1+x^2}\int_{z(w)}^{z_{\text{top}}} \varrho_v \frac{p}{p_0}\,dz\right) dx \tag{19}$$

Following Möller (1944), as will be explained later on, the spectrum is subdivided into numerous intervals each of which may be characterized by a single artificial spectral line. In the ideal case, such a composite spectral line exhibits exactly the same absorption properties as the contribution of all the real lines in the interval. Since the radiative transfer equation pertains to monochromatic radiation only, the transmission function must therefore be computed for each parameter x and is then given as

$$D(w/\mu, x) = \exp\left(-\frac{k_0\,\mu^{-1}}{1+x^2}\int_{z(w)}^{z_{\text{top}}} \frac{p}{p_0}\,\varrho_v\,dz\right) = \exp\left(-\tau_D(x)/\mu\right) \tag{20}$$

Here z_{top} stands for the radiatively effective top of the atmosphere. In order to obtain the total downward flux at the top of the cloud, one must first average the downwardly directed intensities of the diffuse radiation field according to equation (19) for each spectral interval, i.e.

$$I_2^{(m=0)}(T_D, \mu) = \frac{1}{d}\int_0^d I_1^{(m=0)}(T_D(x), \mu)\,dx \tag{21}$$

The total downward flux, according to equation (14) consisting of the sum of diffuse and parallel radiation is then

$$F_2(T_D) = 2\pi\int_0^1 I_2^{(m=0)}(T_D, \mu)\,\mu\,d\mu + \frac{\mu_0}{d}\int_0^d E_R\,e^{-T_D(x)/\mu_0}\,dx \tag{22}$$

where E_R stands for solar intensity at the top of the atmosphere. For ground fog and ground albedo zero, one has at the lower boundary

$$I_1^{(m=0)}(T_E, \mu) = B_G \quad \text{and} \quad F_1(T_E) = \pi B_G \tag{23}$$

where B_G stands for the black body radiation of the ground.

3.3. *The determination of radiative intensities within the cloud*

Equation (12), together with (10) and (11), solve the transfer problem which is considered here. Due to the fact that for a given phase function the quantities $I_{1,0}^{(m)}$, $I_{2,0}^{(m)}$, $R_1^{(m)}$, $R_2^{(m)}$ can be determined, equation (12) is suitable for iterations. The iteration method which is adopted here is explained in section 3.4. In order to begin with the first step in the iteration process, the emission integrals of the long wave radiation in (10) must be evaluated. Instead of evaluating these integrals directly by numerical procedures, it is more convenient to use an analytical method and apply numerical integration procedures at the point that the analysis cannot be carried any further. The coupling of equations (7) and (17) results in the following equations describing the diffuse intensity due to the emission of atmospheric gases and droplets within the m^*th layer as shown in Fig. 3.

$$\begin{aligned}
I_1^{(m=0)}(\tau_E^{(m^*)}, \mu) &= kB_0^{(m^*)} + kB_1^{(m^*)}[\tau_E^{(m^*)} + \mu] \\
&\quad + \{I_1^{(m=0)}(T_E^{(m^*)}, \mu) - kB_0^{(m^*)} - kB_1^{(m^*)}[T_E^{(m^*)} + \mu]\} \\
&\quad \times \exp\left(+(\tau_E^{(m^*)} - T_E^{(m^*)})/\mu\right) \\
I_2^{(m=0)}(\tau_E^{(m^*)}, \mu) &= kB_0^{(m^*)} + kB_1^{(m^*)}[\tau_E^{(m^*)} - \mu] \\
&\quad + \{I_2^{(m=0)}(T_E^{(m^*-1)}, \mu) - kB_0^{(m^*)} + kB_1^{(m^*)}\,\mu\} \\
&\quad \times \exp\left(-\tau_E^{(m^*)}/\mu\right)
\end{aligned} \tag{24}$$

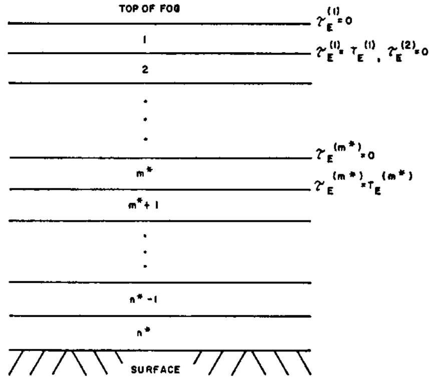

Fig. 3. Distribution of optical depth in E-layer.

The upwardly directed intensity at the upper border and the downwardly directed intensity at the lower border of the m^*th layer are given according to (24) by

$$\begin{aligned} I_1^{(m-0)}(T_E^{(m^*-1)},\mu) &= kB_0^{(m^*)} + kB_1^{(m^*)}\mu \\ &\quad + \{I_1^{(m-0)}(T_E^{(m^*)},\mu) - kB_0^{(m^*)} - kB_1^{(m^*)}[T_E^{(m^*)}+\mu]\} \\ &\quad \times \exp(-T_E^{(m^*)}/\mu) \\ I_2^{(m-0)}(T_E^{(m^*)},\mu) &= kB_0^{(m^*)} + kB_1^{(m^*)}[T_E^{(m^*)}-\mu] \\ &\quad + \{I_2^{(m-0)}(T_E^{(m^*-1)},\mu) - kB_0^{(m^*)} + kB_1^{(m^*)}\mu\} \\ &\quad \times \exp(-T_E^{(m^*)}/\mu) \end{aligned} \tag{25}$$

Here k assumes the following form:

$$k = \frac{\beta_{ABS}(\text{Droplets}) + K_0 \varrho_v \dfrac{p}{p_0}\dfrac{1}{1+x^2}}{\beta_{EXT}(\text{Droplets}) + K_0 \varrho_v \dfrac{p}{p_0}\dfrac{1}{1+x^2}} \tag{26}$$

where k remains sensibly constant throughout the fog layer.

In equation (25) the quantities $I_1^{(m-0)}(T_E^{(m^*)},\mu)$ and $I_2^{(m-0)}(T_E^{(m^*-1)},\mu)$ pertaining to the lower and upper boundaries of the m^*th partial layer of E must now be eliminated. This is accomplished as follows.

To determine the radiative intensity $I_2^{(m-0)}(T_E^{(m^*-1)},\mu)$ one applies (25) to the first partial layer at the upper boundary of the fog and obtains the intensity $I_2^{(m-0)}(T_E^{(1)},\mu)$. From equation (6) one finds the boundary term of this layer whose evaluation is discussed in section 3.2. The intensity $I_2^{(m-0)}(T_E^{(1)},\mu)$ is now used in (25) as the boundary term for the second partial layer to determine $I_2^{(m-0)}(T_E^{(2)},\mu)$ at its lower boundary. This procedure of successive substitution is used to obtain $I_2^{(m-0)}(T_E^{(m^*-1)},\mu)$ which is then substituted into the second equation of (25).

Beginning at the lower boundary of the fog, the corresponding procedure is used to obtain $I_1^{(m-0)}(T_E^{(m^*)},\mu)$ which permits the elimination of this quantity from the first equation of (25). The resulting equations are somewhat lengthy. Therefore, they are not displayed here but are reproduced in detail in appendix 2.

This information permits the determination of the upwardly directed intensity at the upper boundary and the downwardly directed intensity at the lower boundary of the m^*th layer. Furthermore, using the relationships of appendix 2, substituting $m^*=1$ or $m^*=n^*$, and recognizing that $I_1^{(m-0)}(T_E^{(0)},\mu) = I^{(m-0)}(0,\mu)$, one obtains the intensities of the ascending and descending radiation at the upper and lower boundaries of the fog, respectively. In the absence of scattering processes, one may now determine for any value of x and μ the upwardly and downwardly directed intensities at any desired level within the fog. Such detailed procedure is necessary because of the complicated iteration scheme to be discussed in the next section. Moreover, by replacing the suffix E in terms of D, the same equations are used to obtain the intensities of thermal radiation of atmospheric gases outside the cloud or fog layer where $k=1$.

3.4. *The solution of the radiative transfer equation by iteration methods*

With the aid of equations (12) it is possible to develop an iterative procedure in order to obtain the radiative intensities $I_1^{(m)}(\tau,\mu)$ and $I_2^{(m)}(\tau,\mu)$ for $0 \leqslant \tau_E \leqslant T_E$. The following boundary conditions are applied.

$$\begin{aligned} &\tau_E = 0, \quad I_2^{(m)}(\tau_E=0,\mu) = I_2^{(m)}(T_D,\mu) \\ &\tau_E = T_E, \quad I_1^{(m)}(T_E,\mu) = B_G \end{aligned} \tag{27}$$

Inspection of (12) indicates that the functions K_1 and K_2 are independent of the intensities I_1 and I_2 of the diffuse radiation field. Therefore, K_1 and K_2 are suitable as the zeroes approximation. With the aid of the iteration index ν one can write

$$\begin{aligned} I_1^{\nu=0(m)}(\tau,\mu) &= K_1^{(m)}(\tau,\mu) \\ I_2^{\nu=0(m)}(\tau,\mu) &= K_2^{(m)}(\tau,\mu) \end{aligned} \tag{28}$$

The general iteration equations for $\nu = i$ assume the forms

$$\begin{aligned} I_1^{\nu=i(m)}(\tau,\mu) &= K_1^{(m)}(\tau,\mu) \\ &\quad + Q_1^{(m)}(\tau,\mu; I_1^{\nu=i-1(m)}, I_2^{\nu=i-1(m)}) \\ I_2^{\nu=i(m)}(\tau,\mu) &= K_2^{(m)}(\tau,\mu) \\ &\quad + Q_2^{(m)}(\tau,\mu; I_1^{\nu=i-1(m)}, I_2^{\nu=i-1(m)}) \\ &\qquad \nu = 1, 2, \ldots, n \end{aligned} \tag{29}$$

It will be seen that the ith approximation is computed from the $(i-1)$ iteration and the zeroth approximation ($\nu = 0$) which is explicitly included for each ν. The iteration process is physically meaningful. The first substitution means that the primary scattered light and the radiative energy due to the emission of gases and droplets penetrate the entire cloud. Every droplet is therefore illuminated with this radiation and reradiates a certain fraction of the incident radiation. The light which is now available for secondary radiation in direction μ is the primary scattered light illuminating the droplet from all directions μ'. Every continued substitution then includes the effect of one higher order of scattering.

Convergence for all (τ, μ) is assumed if the following inequality is satisfied.

$$\frac{I_j^{\nu-i(m)}(\tau,\mu) - I_j^{\nu-i-1(m)}(\tau,\mu)}{I_j^{\nu-i(m)}(\tau,\mu)} < \varepsilon = 0.01 \quad (30)$$

with $\qquad j = 1, 2$

The reasons leading to the selection of $\varepsilon = 0.01$ are discussed in section 5.

3.5. *Extension of the analysis to the entire spectrum*

The equation of radiative transfer is valid only for monochromatic radiation. The extension of the analysis to the entire spectrum is briefly described next. The infrared spectrum, extending from approximately 3.5 microns to 95 microns is subdivided into 37 intervals, each of which is characterized by constant droplet attenuation coefficients and by the composite spectral line. Since the absorption coefficient of the composite spectral line varies rapidly along the line profile from its maximum value k_0 at the line center to the cut-off point $x = d = 10$ of equation (19), the radiative transfer equation needs to be evaluated for a number of x-values. This is accomplished by subdivision of the spectral line from $x = o$ to $x = d$ into twenty equal intervals. For each value of μ, for a given height above as well as inside the fog, the radiative intensities $I_1^{(m-0)}$ and $I_2^{(m-0)}$ are then evaluated for each of the twenty-one x-values.

The averaging process over a composite spectral line, as indicated by equation (19) or by an equivalent expression involving $I_1^{(m-0)}$, is carried out at all considered heights by means of Simpson's rule. Numerical tests indicate that a subdivision of the spectral line into more than twenty intervals does not result in noticeable improvement. Indeed, a subdivision into ten equal intervals gives already acceptable results.

Next, the spectrally averaged values are integrated over angular distances according to equations (13, 22) to obtain spectrally averaged fluxes. These fluxes are multiplied by the proper band widths of each spectral sub-region. Results for the total infrared spectrum are then obtained by summation of fluxes over all 37 spectral intervals.

Similarly, the solar spectrum, extending from approximately 0.28 microns to 3.5 microns, is subdivided into 15 spectral intervals. The partition occurs in such a manner that occurring water vapor absorption bands are not separated. Each one of the sub-regions is characterized by constant droplet attenuation coefficients. For those regions containing a water vapor absorption band, the composite spectral line parameters are provided also. The averaging process and the integration over the entire solar spectrum is analogous to the procedure adopted for the infrared spectrum.

4. Radiative input parameters

In the light of the preceding discussion it is evident which quantities must be known for the evaluation of the radiative transfer equation. These are

$\beta_{EXT}, \beta_{SCAT}, \beta_{ABS}$:	the volume extinction, scattering, and absorption coefficients
k_0:	maximum absorption coefficients of composite spectral lines
$p(\cos\theta)$:	the normalized phase function
p_l:	coefficients used to expand the phase function into a series of Legendre polynomials

These quantities are of primary physical importance and are only obtainable after complicated and laborious computations. More or less sporadic data available in the literature, often in unusable graphic format, are not sufficient to satisfy the requirements of this study. A brief discussion on the input parameters will be given next. For details see Zdunkowski & Strand

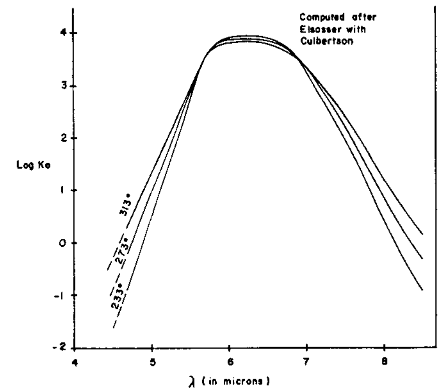

Fig. 4. Maximum absorption coefficients of composite spectral lines for 6.3 microns water vapor band.

(1969). All arising Mie computations are carried out in an exact manner with locally developed Fortran programs.

The spectrum ranging from 0.28 μ to 95 μ is divided into fifty-two intervals. Fifteen of these spectral regions pertain to the solar spectrum, which is subdivided in such a manner that occurring absorption bands are not separated. For wave length less than 1 μ, the absorption data by Fowles (see *Linkes Meteorologisches Taschenbuch*, 1953), for the spectral region from 1 μ to 4.25 μ, the absorption data of Wyatt *et al.* (1962) and for wavelengths larger than 4.25 μ the absorption data tabulated by Elsasser & Culbertson (1960) are utilized to obtain k_0 values. Least square computations indicate that $d = 10$ gives the best fit. Some of the results of the k_0 computations are shown in Fig. 4. Computations of the droplet attenuation coefficients are based upon the indices of refraction of pure water. The real part of the refractive index for $0.3\ \mu \leqslant \lambda \leqslant 0.7\ \mu$ is taken from *Linkes Meteorologisches Taschenbuch II* (1957). Corresponding imaginary parts are computed from absorption data provided in the *Smithsonian Meteorological Tables*. For wavelengths from $0.7\ \mu \leqslant \lambda \leqslant 3.75\ \mu$ the new tabulations of Irvine & Pollack (1968) are utilized, while for $\lambda > 3.75\ \mu$ the indices of refraction of McDonald (1960) and Herman (1962) are taken into account.

The evaluation of the attenuation parameters for a unit element of cloud air, containing the entire spectrum of droplets of radii r, requires the specification of the droplet size distribution function $n(r)$. Based on numerous measure-

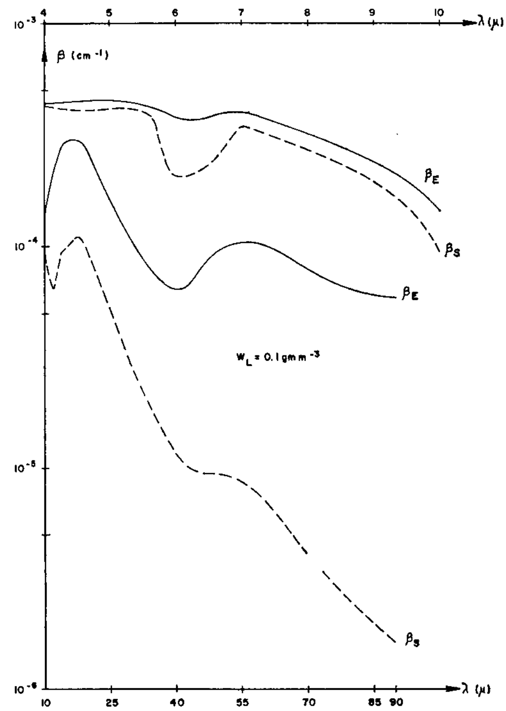

Fig. 5. Distribution of attenuation coefficients in cm^{-1}.

ments of liquid water content and droplet sizes of layer clouds and fogs, Best (1951) proposes the following interpolation formula in terms of the total liquid water content W_L,

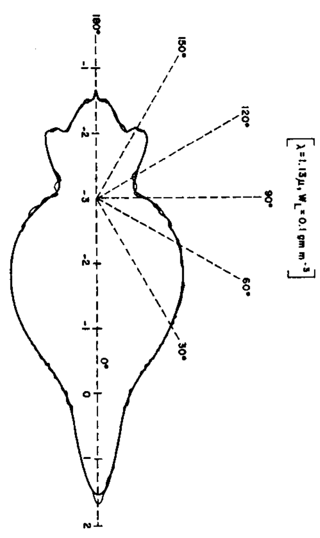

Fig. 6. Analytic representation of phase function at 1.13 microns, radius vector on logarithmic scale.

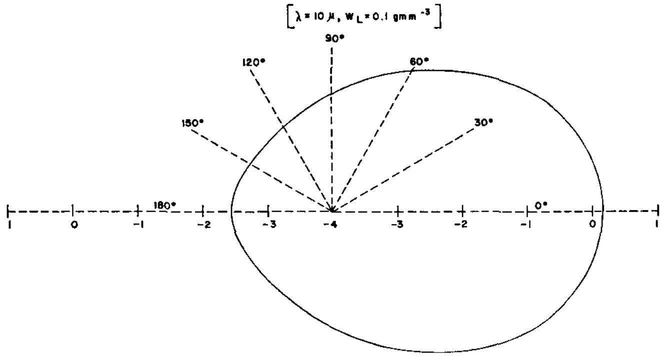

Fig. 7. Angular distribution of scattered infrared light at 10 microns, radius vector on logarithmic scale.

$$n(r) = \frac{12.605\, W_L \cdot 10^6 (2\bar{r})^{-0.7}}{\omega_L^{3.3}} \exp\left\{-\left(\frac{2r}{\omega_L}\right)^{3.3}\right\},$$
$$(\mathrm{cm}^{-3} \Delta r^{-1}) \tag{31}$$

Here $\bar{r}$ is the mean radius of size increment. The quantities W_L(g/m³) and ω_L (microns) are related by means of

$$W_L = 1.1 \cdot 10^{-3} \omega_L^{1.79}$$

The attenuation parameters are then evaluated for a liquid water content of 0.1 g/m³ which is thought to apply to a fog. Denoting with Q_S the scattering efficiency factor, the volume scattering coefficient can be written as

$$\beta_S = \pi \int_0^{r_1} n(r)\, r^2 Q_S(r)\, dr \tag{32}$$

Similar expressions are valid for absorption and extinction. The upper limit $r_1 = 15$ microns, is the largest radius still contributing to the integral. For this value, the droplet number density is less than 10^{-10} particles/cm³. The distribution of β_S ad β_E for the infrared spectrum is shown in Fig. 5.

As soon as β_S is known, the phase functions for scattering angle θ are obtained in terms of the Mie intensity functions i_1 and i_2. This is accomplished by means of

$$\frac{p(n(r), \theta)}{4\pi} = \frac{1}{2\beta_S k_*^2} \int_0^{r_1} (i_1(\theta) + i_2(\theta))\, n(r)\, dr \tag{33}$$

where $k_* = 2\pi/\lambda$.

Two sample phase functions are depicted in Figs. 6 and 7. The radius vectors representing the scattered light are shown on a logarithmic scale. The ratio of forward to backward scattering is nearly four orders of magnitude for the short wave side of the solar spectrum but decreases with increasing wavelength. The pronounced lobes of the solar spectrum phase function have completely disappeared in the infrared range. The undulating line of Fig. 6 approximating the solid line, represents the analytical approximation of the phase function. The approximation requires about 150 terms of the Legendre expansion. At 10 μ the approximation curve and the phase function nearly coincide. Only fifteen terms are needed for the expansion. The expansion procedure, together with some numerical details, is described in appendix 3.

5. Convergence and limiting cases

The reliability of the computational procedure will be checked now by considering two limiting cases. First, a spectral interval in the solar spectrum is chosen where no absorption processes are taking place. In such a region, the expansion of the phase function into a Legendre series requires approximately 150 terms. If numerical inaccuracies occur, they will be most noticeable in this spectral interval since more than 100 scattering processes take place till the condition on ε is satisfied. The flux divergence pertaining to a non-absorbing medium equals zero. From this follows that the sum of the fluxes, including the direct still parallel solar radiation, must remain constant with height. This condition is found to be satisfied with a high degree of precision for $\varepsilon = 0.01$ while for a somewhat larger ε value, constant net flux is not obtained. Indeed, all computations are checked to see if constant net flux with height is obtained by setting temporarily all absorption coefficients equal to zero. Now illumination of the fog takes place only by parallel solar radiation and the black body radiation of the ground. It should be noted that constant net flux is obtained only then, if integration over angles and optical path length takes place over sufficiently dense intervals. Having found optimal conditions for the time consuming integrations, the true absorption coefficients for water vapor and droplets are introduced into the solution equations to carry out the required computations.

Having established the accuracy of the flux computations in case of purely conservative processes, the accuracy of the absorption calculations must be tested by considering a second limiting case.

Temporarily setting the scattering coefficients equal to zero, fluxes and their divergences due to water vapor and water droplets absorption and emission are obtained and compared with results obtained using conventional methods (see, for example, Zdunkowski, 1963). Again excellent agreement is found for all test cases.

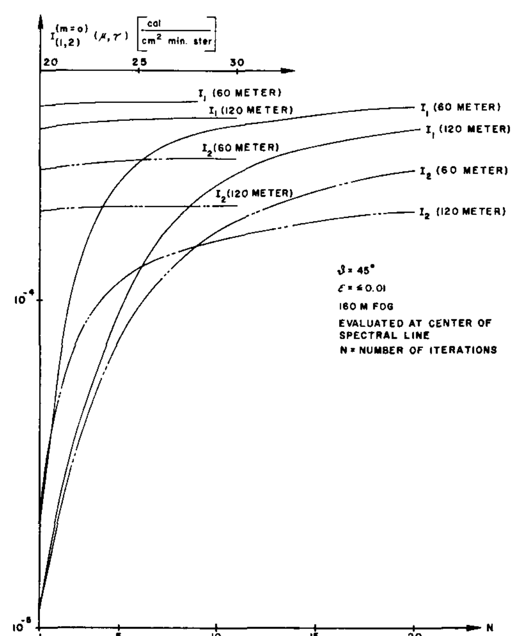

Fig. 8. Convergence test at 4 microns.

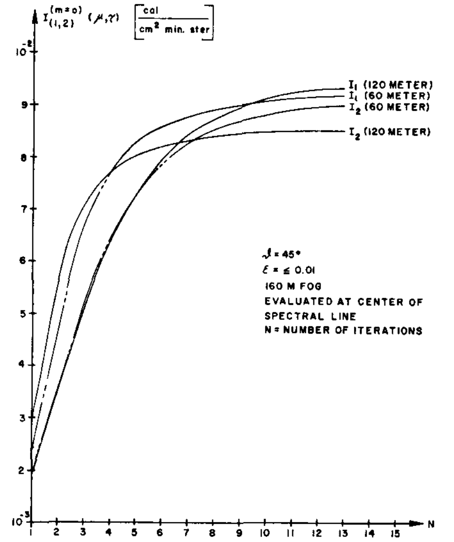

Fig. 9. Convergence test at 8.5 microns.

Finally, if both absorption and scattering processes are taking place, convergence is best observed by considering upwardly and downwardly directed intensities for a given height and direction as function of the number of iteration processes to satisfy the condition $\varepsilon = 0.01$.

This is demonstrated in Figs. 8 and 9 for wavelengths 4 and 8.5 microns in case of a fog extending to a height of 160 meters. Iteration number one corresponds to the zeroth approximation. As will be seen, the intensities increase rapidly due to lower order scattering and reach saturation values with an increasing number of scattering processes without showing any noticeable oscillations.

It is interesting to observe the sensitivity of the numerical solution to the choice of ε. Consider again Fig. 8 which pertains to a wavelength of 4 microns. A choice of $\varepsilon = 0.02$ discontinues the iteration process after 23 iterations. Inspection shows that the intensities have not quite reached saturation values. Taking $\varepsilon = 0.01$ requires 30 iterations while a choice of $\varepsilon = 0.001$ discontinues the iteration process after 57 iterations. A choice of $\varepsilon = 0.001$ instead of $\varepsilon = 0.01$ triples computer time without significantly improving the accuracy of the computations. For a wavelength of 8.5 microns, a choice of $\varepsilon = 0.02$ requires 7 iterations. Inspection of Fig. 9 indicates that the intensities have not reached saturation values. For $\varepsilon = 0.01$,

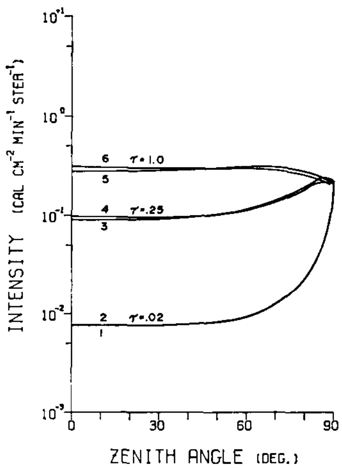

Fig. 10. Comparison of downwardly directed intensities at the surface of the earth as computed by the iterative and exact methods for a Rayleigh atmosphere and $\mu_0 = 1.00$.

saturation is reached requiring 13 iterations while 24 iterations are needed to satisfy the condition $\varepsilon = 0.001$. Again, computer time is tripled by choosing $\varepsilon = 0.001$ instead of $\varepsilon = 0.01$ without significantly improving the accuracy of the computations. Further test computations, not reported, for different wavelengths and different points along the spectral line indicate that the choice of $\varepsilon = 0.01$ is sufficient for all practical purposes.

An additional appraisal of the accuracy of the method is obtained by applying the solution scheme to the solar spectrum and the conservative Rayleigh atmosphere. For this idealized atmosphere, due to the simplicity of the phase function, an exact solution of the radiative transfer equation is known which takes into account all orders of scattering as well as polarization effects. Results are tabulated by Coulson *et al.* (1960) who used the molecular optical thicknesses obtained by Deirmendjian (1955) on the basis of the Rand model. Using the data of the same model (Grimminger, 1948) to match the tabulated optical thicknesses, a comparison is made between the results obtained with the present and the exact solutions for $\varphi - \varphi_0 = 0$.

Fig. 10 shows the distribution of the downwardly directed intensities at the surface of the earth, as computed by both methods, for a solar zenith angle of zero degrees and zero ground reflection. For a small optical thickness, $\tau = 0.02$, the present and the exact methods give nearly identical results as evidenced by curves 1 and 2. The intensities pertaining to two larger optical path lengths, curves 3 and 5 (present method) and curves 4 and 6 (tabulated values) show reasonably small deviations. Moreover, the deviations are not systematic since the intensity curves cross each other. Radiative fluxes (not shown), the quantities of main meteorological interest in heat budget considerations, are nearly identical.

Fig. 11 refers to the same conditions but to a solar zenith angle of approximately 66.4 degrees. For $\tau = 0.02$, curves 1 and 2, both methods yield identical results. Deviations are reasonably small for the larger optical path lengths as depicted by curves 4 and 6 (present method) and curves 3 and 5 (tabulated values). It is noted that the total atmospheric optical thickness values of 0.02 and 1.00 of the Rayleigh atmosphere refer to the wavelengths of 0.8090 and 0.3020 microns, respectively. These are the smallest and largest optical path lengths for which the intensities are tabulated.

The distribution of upward and downward intensities at the upper and lower boundaries of the atmosphere is displayed in Fig. 12 for $\tau = 0.25$ and $\mu_0 = 1$. The effect of a uniform ground albedo A is considered in some instances. Curves 1 (present method) and 2 (tabulated values) show the upward intensities at the top of the atmosphere for $A = 0$. The small devia-

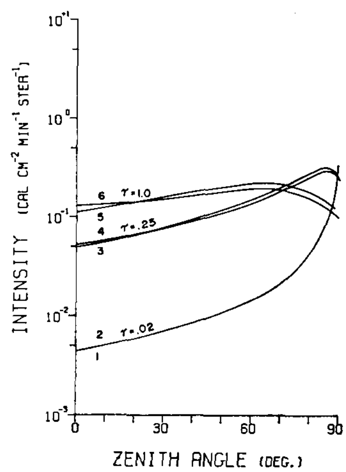

Fig. 11. Comparison of downwardly directed intensities at the surface of the earth as computed by the iterative and exact methods for a Rayleigh atmosphere and $\mu_0 = 0.40$.

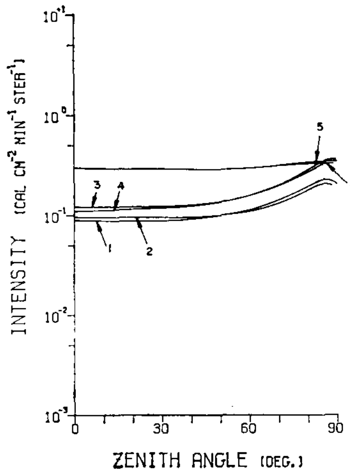

Fig. 12. Comparison of the upwardly and downwardly directed intensities for a Rayleigh atmosphere as computed by the iterative and exact methods with ground reflections of zero and 0.25.

tions resulting from the two computational methods are even less significant if $A = 0.25$, as is apparent from curves 5 (present method) and 6 (tabulated values). The downwardly directed intensities at the surface of the earth for $A = 0.25$ are shown by curves 3 (tabulated values) and 4 (present method). Again, deviations resulting from the exact and the iterative methods are very small.

It is known that the Rayleigh atmosphere is particularly sensitive to polarization effects due to the shape of the Rayleigh phase function. The deviations of the two methods are attributed to polarization which is disregarded in the iterative scheme. Figs. 10, 11 and 12 are computed for $\varepsilon = 0.001$. Results do not differ significantly using the somewhat less restrictive value of $\varepsilon = 0.01$.

6. Results

6.1. *General remarks*

The computations deal with two fog models, a low fog extending to 160 cm and a high fog extending to 160 m. In both cases a liquid cloud water content of 0.1 gram per cubic meter, a value representative of stratus clouds, and saturation vapor pressure with respect to a flat water surface are assumed to exist within the fog. The sounding used in these computations is constructed in the lower part of the atmosphere but corresponds to average conditions at temperate latitudes above the height of 1 kilometer as recorded by London (1950). The temperature distribution is assumed to be the same in both cases. Details are shown in Fig. 13.

Computations are carried out for the entire infrared spectrum which extends from 2.5 to 95 microns. As far as the solar spectrum is concerned, calculations are carried out to the extent only as to test the applicability of the flux method.

The solar spectrum stretches from 0.28 microns to 4.75 microns. In the infrared part of the solar spectrum, the radiative transfer equations are not entirely decoupled from thermal emission since beyond 2.5 microns the thermal emission of water vapor and droplets becomes noticeable.

In the following it should be noticed that for the solar spectrum the intensities are only evaluated for $m = 0$, which is the *only* component contributing to the radiative fluxes as defined in equations (15) and (16). Since in the case of infrared radiation, $m = 0$ is the only intensity which is defined, plots of intensity represent true distributions. This is not the case in the solar spectrum where by equation (5) the term $m = 0$ is only the leading term in the expansion of the total intensity. The true distribution of

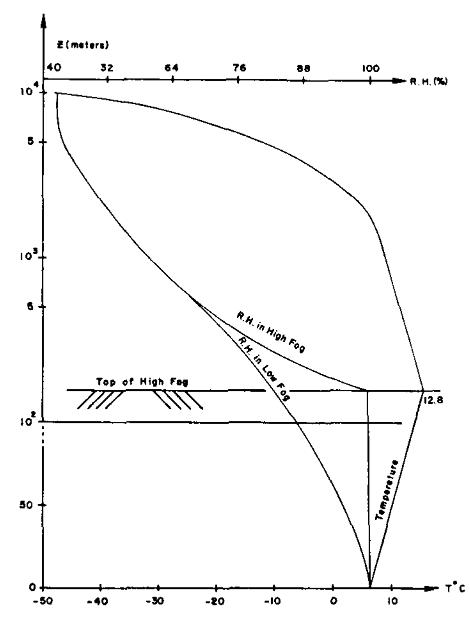

Fig. 13. Temperature and humidity distributions.

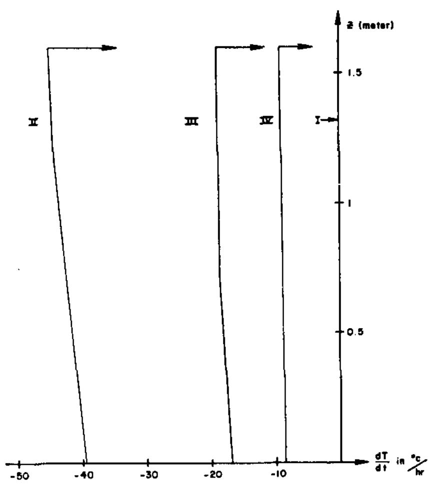

Fig. 14. Radiative temperature change in low fog.

the intensities can only be obtained by summing over all terms in the expansion. Results will be made available in a future paper.

6.2. *Distribution of infrared radiation in low fog*

The temperature distribution of Fig. 13 is used now to discuss radiative temperature changes in low fog pertaining to the entire infrared spectrum. Due to the presence of water vapor alone, the temperature change is very small as indicated in Fig. 14, case I. The cooling curve coincides practically with the ordinate of the diagram and is not shown.

Next, consider the hypothetical case II that the fog consists of water droplets only obeying the adopted size distribution function. Above the fog a vacuum is assumed to exist. Furthermore, all scattering effects of the droplets are presently neglected so that the extinction of the droplets is described entirely by the absorption coefficient. In contrast to the previous case, the upwardly directed radiation is only weakly compensated by the downwardly directed flux. This results in an extremely fast increase of the net radiation which causes an average value of radiative cooling of more than 42 degrees per hour.

Now consider the total effect of water vapor and non-scattering but absorbing fog droplets depicted as case III. As expected, the temperature change distribution curve is found to be located between the corresponding curves of the previously discussed limiting cases. Finally, consider the general case IV which takes into account the absorption of water vapor and droplets as well as multiple scattering. The temperature profiles of cases III and IV are similar in shape but differ strongly in magnitude as expected. Repeated scattering causes a considerable increase of the traversed path of radiation inside the fog layer. This results in larger net absorption rates thus preventing the extreme cooling as discussed in conjunction with the simplified case III. The importance of including the effect of multiple scattering in radiative temperature computations pertaining to low fog is evident. A physical interpretation of the effect of radiative cooling upon the growth of fog is given later on.

The computations give some interesting information about the black body characteristics of a thin fog layer. For this purpose, consider Fig. 15 which shows the distribution of the upwardly and downwardly directed intensities as a function of wave length for a zenith angle of zero degrees. As expected, the distribution of the upwardly directed intensities follows the black body curve of the earth's surface. The downwardly directed intensities are shown for the top of the fog and for the ground. The

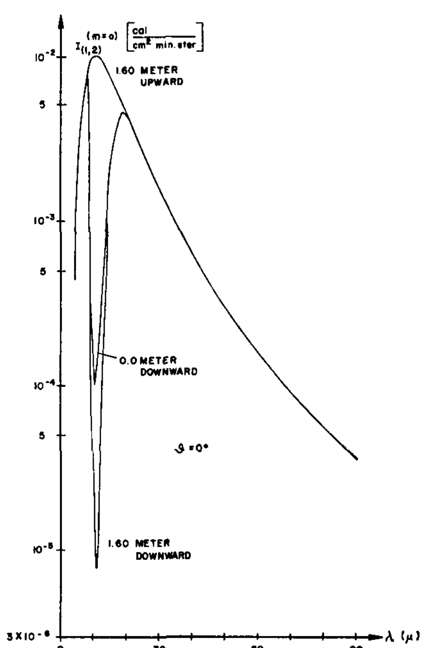

Fig. 15. Distribution of intensities for zenith angle of 0 degrees in 1.60 m fog.

presence of this thin fog increases in the water vapor window the downward radiation by about one order of magnitude. Due to the small vertical extent of the ground fog, black body radiation is not observed. Outside the water vapor window, the strong absorption bands of the atmospheric gases exhibit almost perfect black body radiation. Upwardly and downwardly directed intensities coincide nearly in magnitude.

Fig. 16 gives the variation of the downwardly directed intensities in the water vapor window. With increasing zenith angle and decreasing height, intensities increase rapidly. Black body energy corresponding to the given temperature distribution is observed for horizontal view. This, of course, is to be expected since the fog is assumed to extend infinitely far in horizontal direction. The strong intensity variation as a function of the zenith angel indicates that the fog is still far removed from being a black body, since a black body fog would be characterized by horizontal distribution lines of the downwardly directed intensities. Upwardly directed intensities are not shown since they are represented by nearly coinciding horizontal lines corresponding in magnitude to the black body intensity of the earth.

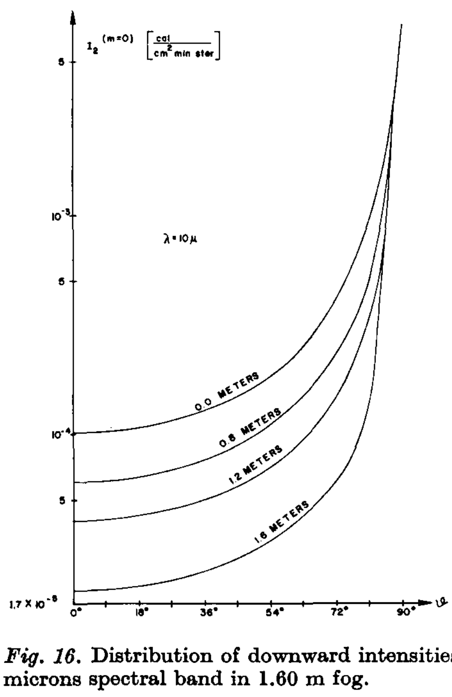

Fig. 16. Distribution of downward intensities of 10 microns spectral band in 1.60 m fog.

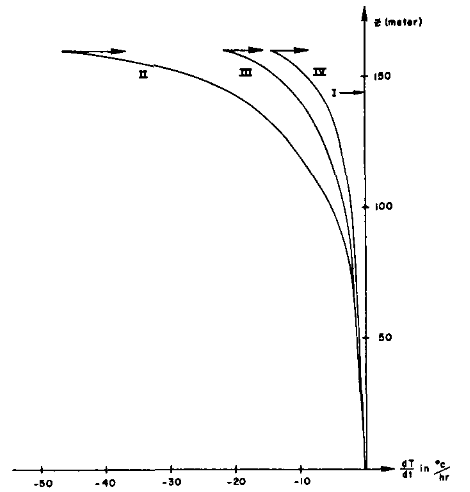

Fig. 17. Radiative temperature change in high fog.

6.3. *Distribution of infrared radiation in high fog*

The temperature and moisture distribution of Fig. 13 is used now to determine the total infrared cooling rate in high fog. This is shown in Fig. 17. The case labeling is identical to that in low fog as described in section 6.2. Due to the large vertical extent of the droplet layer, the lower section of the fog acts nearly as a black body thus preventing strong radiative temperature changes. This black body behavior does not exist in the upper fog region where the upwardly and downwardly directed components of the radiative flux are strongly unbalanced.

The radiative temperature change due to water vapor alone (case I), as in low fog, is very small so that the cooling curve practically coincides with the ordinate of the diagram. The effects of water droplets alone (case II) as well as the combined action of water droplets and water vapor (case III) result in larger temperature changes than the corresponding values pertaining to low fog. In the general case IV which includes multiple scattering, the radiative temperature change at the top of the high fog exceeds the corresponding value for low fog by nearly a factor of two. Again it is evident from inspection of Fig. 17 that the effect of multiple scattering upon radiative temperature changes must not be disregarded.

Radiative effects upon fog growth can now be estimated. The strong cooling rates in the top layer of the fog cause supersaturation with subsequent formation of more droplets. Hence,

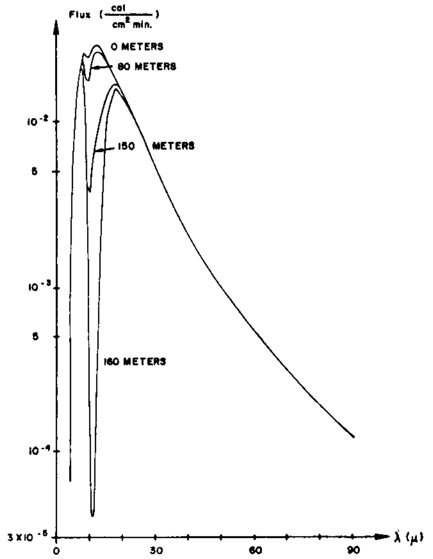

Fig. 18. Distribution of diffuse downward fluxes in 160 m fog.

the fog increases in density. Turbulence carries the droplets across the upper fog boundary which often results in nearly explosive vertical growth of the fog. If the fog initially is not growing in vertical thickness due to the absence of exchange processes, strong superadiabatic temperature gradients must result from radiative cooling. These cannot be maintained for any extended period of time and give cause to new turbulence.

Next some spectral flux properties of high fog are discussed. Fig. 18 shows the distribution of downwardly directed fluxes at various heights. Fluxes, as before, are obtained by integrating over all directions and over the distribution of the absorption coefficients of each spectral line. In the near and far infrared absorption bands of water vapor, the flux curve definitely shows black body behavior. Due to multiple scattering processes, the downwardly directed flux at a given reference height contains some energy which originated below this reference level. Due to the fairly small temperature range within the fog, one single curve is sufficient to describe the downwardly directed flux at all levels outside the water vapor window. The window region, however, shows up very prominently at the top of the fog, since here the downward flux of the atmospheric water vapor is extremely weak. At a height of 150 m the gap in the window is almost closed due to the presence of water droplets. A further increase of droplet optical path length results in increased radiation, so that the surface of the earth nearly receives black body energy corresponding to some mean temperature of the fog. This is equivalent to stating that a stratus cloud of 160 m of thickness, to a good approximation, may be considered to be a perfect black body.

Upwardly directed fluxes are not shown since black body behavior is found for all wave length due to the presence of the earth's surface.

Very instructive is an investigation of the magnitudes of the downwardly directed intensities in the water vapor window. Some computational results representing the wave length region from 9.75 to 10.25 microns are shown in Fig. 19. For small zenith angles the intensities at the top of the fog are extremely small. For horizontal view, of course, black body energy is observed due to the infinitely large horizontal extent of the fog. With decreasing height, i.e., with increasing optical thickness, the downwardly directed intensities increase rapidly in magnitude even for very small zenith angles. In the lower part of the fog, the dependency of the intensity on zenith angle has nearly disappeared as the intensity lines become nearly horizontal in the neighborhood of the earth's surface. This indicates that a fog of 160 m of thick-

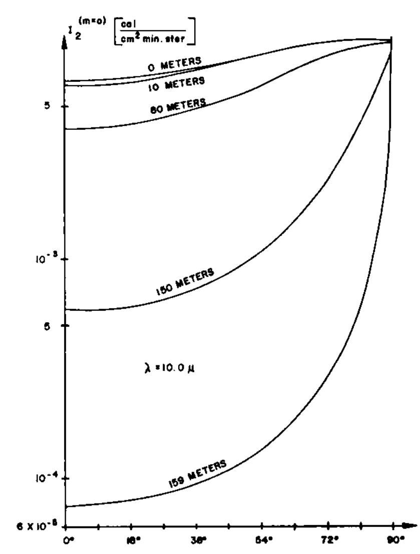

Fig. 19. Distribution of downward intensities of 10 microns spectral band in 160 m fog.

ness in this spectral region can be thought of as a black body of some representative temperature observed within the fog.

For the strong infrared absorption bands of water vapor, no intensity distributions will be shown. Black body radiation is observed which results in nearly horizontal intensity distribution lines. The distribution of the downwardly directed intensities pertaining to spectral regions which are located at the edges of the water vapor absorption bands show a behavior entirely analogous to that shown in Fig. 19. Due to the presence of the earth's surface, the upwardly directed intensities do not exhibit any prominent features and are left out of the discussion. They are simply represented by straight lines.

6.4. *Distribution of solar radiation in low fog*

For heat budget considerations, one is mostly interested in obtaining radiative fluxes. Hence it is only necessary to obtain the intensity components for $m = o$. Intensities of the other components ($m \neq o$) do not contribute to the fluxes since they disappear when the integration over all directions is performed.

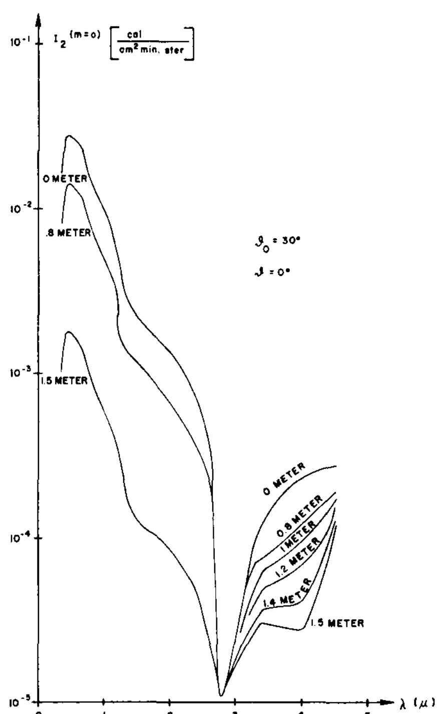

Fig. 20. Distribution of downward intensities in 1.60 m fog.

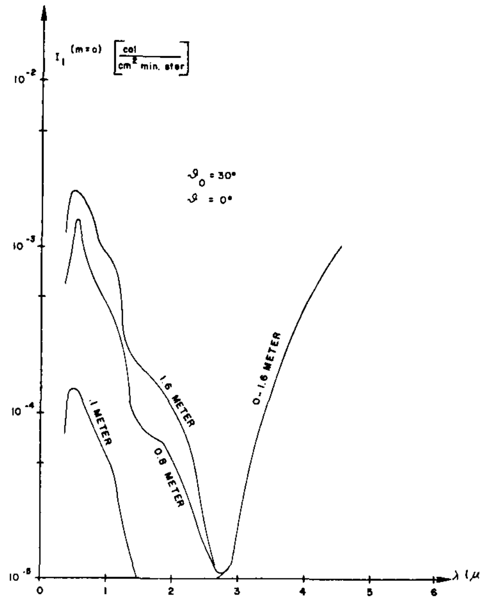

Fig. 21. Distribution of upward intensities in 1.60 m fog.

Consider the distribution of the downwardly and upwardly directed to the flux contributing intensities as a function of wave length for solar and observational zenith angles of 30 and 0 degrees respectively. The contribution of the parallel solar radiation is not included. The results are shown in Fig. 20. As will be seen, the

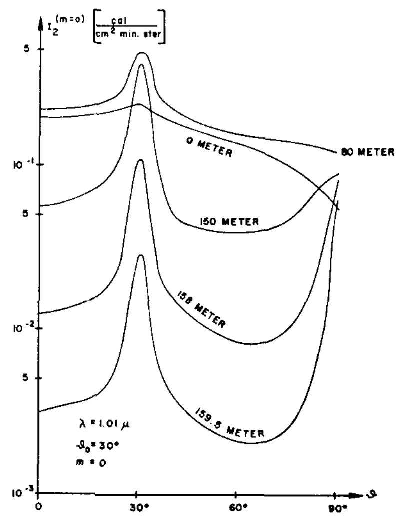

Fig. 22. Distribution of Downward intensities of 1.01 microns spectral band in 160 m fog and solar zenith angle of 30 degrees.

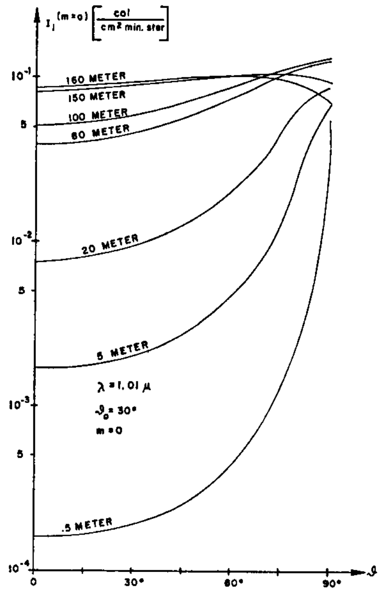

Fig. 23. Distribution of upward intensities of 1.01 microns spectral band in 160 m fog and solar zenith angle of 30 degrees.

downwardly directed intensity component increases with decreasing height for wave lengths less than 3 microns. This is to be expected since with the decrease of the direct, still parallel solar radiation, the diffuse radiation field will increase in magnitude. For wave length longer than three microns, thermal radiation becomes effective which results in an increase of energy for longer wave lengths. The upwardly directed intensity must show the opposite trend for wave length of less than three microns, as demonstrated in Fig. 21, due to the adopted boundary conditions.

The distribution of the intensities as a function of height and zenith angle for a given solar distance in low fog is very similar to that in high fog. For this reason angular distributions are only shown for high fog.

6.5. *Distribution of solar radiation in high fog*

Since presently results are not available for the entire solar spectrum, a somewhat centrally located wave length interval extending from 0.99 to 1.03 microns is used for the sake of discussion. This particular spectral region does not contain an absorption band. The results, however, are typical for other spectral intervals also.

First consider Fig. 22 which gives for a solar zenith angle of 30 degrees the distribution of the downwardly directed to the flux contributing intensities. The direct solar radiation, as before, is not included. Because of $m = o$ a dependency on the azimuth does not exist. One recognizes strong forward scattering in the direction of the parallel solar radiation at a zenith distance of 30 degrees. The maximum value of the intensity is not found near the earth's surface but in the central part of the fog. In this region the direct solar radiation has been nearly extincted so that a further increase of the downwardly directed radiation field cannot take place.

Fig. 23 gives the distribution of the upwardly directed intensities. According to the boundary conditions, the intensity is zero directly at the earth's surface. Intensities increase with increasing height and increasing zenith angle. The strong maximum observed in Fig. 22 is missing. The reason for this is the weak backward scattering. The strong increase of the intensity values with increasing zenith angle at small heights is explained by the increasing thickness

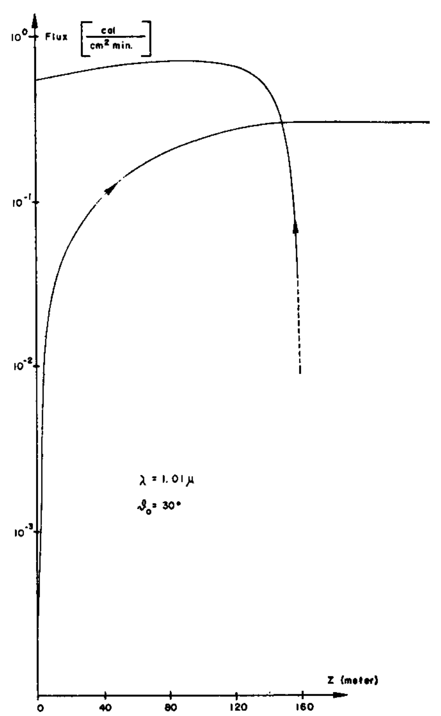

Fig. 24. Distribution of diffuse fluxes of 1.01 microns spectral band in 160 m fog.

of the fog. In the limiting case, at a zenith distance of 90 degrees, the fog is extended infinitely far so that a large number of scattering processes contribute. At this particular zenith angle the upwardly and downwardly directed intensities are the same.

The diffuse fluxes corresponding to the previously shown intensities are depicted in Fig. 24. It will be noticed that the upwardly as well as the downwardly directed fluxes have non-zero values. It is understood that these fluxes refer to energy transports as the boundaries are approached from inside the fog. The downwardly directed radiation has its maximum value at a height of approximately 80 m. At this place the direct solar radiation is nearly completely attenuated so that the diffuse radiative flux cannot increase further. The upwardly directed radiation increases in the same measure as the downwardly directed diffuse radiation field is developed.

For comparison purposes, the flux contributing intensities for a solar zenith angle of 70 degrees are shown in Figs. 25 and 26. Noticeable

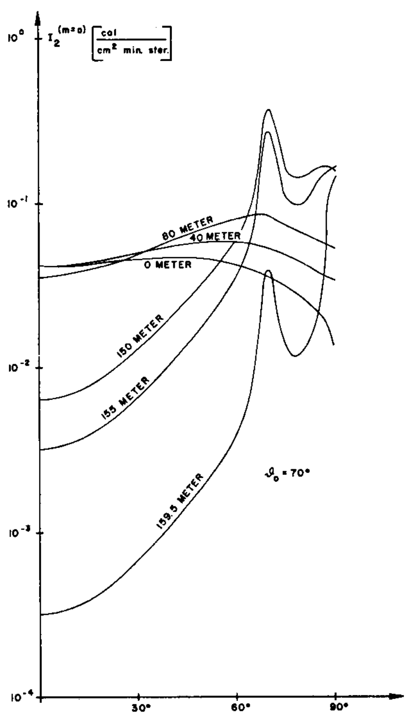

Fig. 25. Distribution of downward intensities of 1.01 microns spectral band in 160 m fog and solar zenith angle of 70 degrees.

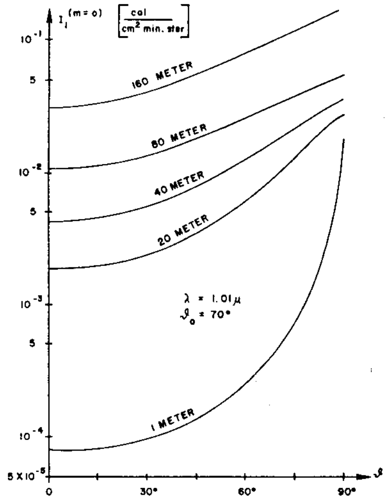

Fig. 26. Distribution of upward intensities of 1.01 microns spectral band in 160 m fog and solar zenith angle of 70 degrees.

is that the maximum value of the forwardly scattered energy in the direction of the zenith distance of the sun is not nearly as pronounced as before. The strong increase of the intensity with increasing zenith distance is masking this effect. The upwardly directed intensities show the same regular behavior as observed for the zenith angle of 30 degrees.

7. Summary and concluding remarks

The radiative transfer equation has been solved and evaluated taking into account the emission and absorption of water droplets and vapor in addition to multiple scattering of water droplets. The exact structure of spectral lines is included in the analysis. The solution method consists of an iterative procedure which is extremely effective in the long wave part of the spectrum for the determination of infrared intensities and fluxes. The method is also very useful for the determination of fluxes in the solar spectrum but has not been tested in case of solar intensities. For flux computations only the leading term of the intensity expansion equation is needed, which is the only term contributing to infrared intensities. The analysis takes into account that solar radiative effects as well as true emission may take place in the same spectral region. An arbitrary splitting of the heat spectrum into two major spectral regions of emission and of no emission, as sometimes suggested, is not necessary using the present method.

Two model fogs are discussed in this study. Using a particular droplet distribution function, radiative intensities, fluxes and flux divergence are computed for the entire infrared spectrum. More than forty different phase functions are used to describe the variation of scattering properties as a function of wave length. This makes the present treatment unique.

Similar investigations are carried out by Russian authors (Feigel'son, 1964) using much more restricted assumptions, such as grey water vapor absorption coefficients and uniform droplet radii. Their results are based upon different atmospheric conditions that comparisons of computational results are rendered impossible. Yamamoto *et al.* (1966) carried out some interesting computations pertaining to radiative processes in a water cloud for the atmospheric window using an averaged scattering function. In this case the influence of water vapor emission can be neglected. Their solution method is based upon an entirely different principle which does not permit statements about the distribution of radiative energy inside the cloud but only at the boundaries.

It appears that the problem of the infrared radiative exchange in a stratus cloud or a fog of approximately 200 m of thickness can be considered as solved by means of this investigation. The computational method is also usable to obtain fluxes in the solar spectrum. Future research will indicate if the method is suitable also to obtain the distribution of solar intensities in a cloud of 200 m of thickness. Furthermore, it must be tested what the limiting cloud thickness is for which the present method is still applicable.

Acknowledgement

The authors are indebted to the United States Army Signal Electronics Command, Fort Monmouth, New Jersey, for sponsoring this research. Gratitude is expressed also to Devon Mecham, a graduate student of the Computer Science Department of the University of Utah, for aiding with the programming part of this research.

REFERENCES

Best, A. C. 1951. Drop-size distribution in cloud and fog. *Q. J. Royal Meteorol. Soc.* 418.

Chandrasekhar, S. 1960. *Radiative Transfer*, pp. 1–12, 149–151. Dover Publications, Inc., New York.

Coulson, Kinsell L., Jitendra, V. Dave & Zdenek, Sekera 1960: *Tables Related to Radiation Emerging from a Planetary Atmosphere with Rayleigh Scattering*, 548 pp. University of California Press, Berkeley and Los Angeles.

Deirmendjian, D. 1955. The optical thickness of the molecular atmosphere. *Archiv Meteor., Geophys. u. Bioklim.*, Serie B, *6*, 452.

Elsasser, W. M. & Culbertson, M. F. 1960. Atmospheric Radiation Tables, *Meteorological Monographs 4*, 23.

Feigel'son, E. M. 1964. Light and heat radiation in stratus clouds. (Translated from Russian.) US Dept. of Commerce, Clearinghouse for Federal Scientific and Technical Information, TT 66-51014.

Grimminger, G. 1948. *Analysis of the Temperature, Pressure and Density of the Atmosphere Extending to Extreme Altitudes.* The Rand Corporation, Santa Monica.

Herman, B. M. 1962. Infrared absorption, scattering, and total attenuation cross-sections for water spheres. *Q. J. Royal Meteorol. Soc. 88*, no. 376, 143–150.

Irvine, W. M. & Pollack, J. B. 1968. Infrared optical properties of water and ice spheres *Internat. J. of Solar System 8*, no. 2, 324–360.

Kraus, H. 1958. Untersuchungen über den nächtlichen Energietransport und Energiehaushalt in der bodennahen Luftschicht bei der Bildung von Strahlungsnebeln. *Ber. Dtsch. Wetterd.*, no. 48.

Linkes Meteorologisches Taschenbuch, II, 1953. Franz Baur, Akademische Verlagsgesellschaft Geest & Portig K.-G., Leipzig, Germany.

London, J. 1950. US Air Force Cambridge Research Laboratory Progress Reports 131.01. 131.02, and 131.03.

McDonald, J. E. 1960. Absorption of atmospheric radiation by water films and water clouds. *J. Meteor. 17*, 232–238.

Möller, F., 1944: Grundlagen eines Diagramms zur Berechnung langwelliger Strahlungsströme. *Meteorologische Zeitschrift 61*, 37–45.

Rodhe, B. 1962. The effect of turbulence on fog formation. *Tellus 14*, 49–86.

Smithsonian Meteorological Tables, prepared by Robert J. List, Washington, D.C., Smithsonian Institution, 1958.

Whittaker, E. T. & Watson, G. N. 1946. *A Course of Modern Analysis*, Chapter 15. University Press; Cambridge, Macmillan, New York.

Wyatt, P. J., Stull, V. R. & Plass, G. N. 1962. Infrared absorption of water vapor. Infrared Transmission Studies Final Report, vol. II.

Contract no. AF 04(695)-96, Geophysics Research Directorate, Air Force Cambridge Research Laboratories.
Yamamoto, G., Tanake, M. & Kamitani, K. 1966. Radiative transfer in water clouds in the 10-micron window region. *J. Atmos. Sci. 23*, no. 3, 305–313.
Zdunkowski, W. 1963. Untersuchungen über die langwellige Strahlung der Atmosphäre. *Ger. Beit. Geophys. 72*, 103–106.
Zdunkowski, W. & Strand, R. 1969. Light scattering constants for a water cloud. *Pure and Appl. Geophys. 19*, 82–105.
Zdunkowski, W. & Nielsen, B. 1969. A preliminary prediction analysis of radiation fog. *Pure and Appl. Geophys. 19*, 45–66.

APPENDIX 1

The evaluation of the equations (9) for the detemination of the primary scattered light of the solar radiation in fog requires the treatment of several special cases; these are listed next.

I. $\mu=\mu_0$: $$I_{2,0}^{(m)}(\tau,\mu)=\frac{(1-k)}{4\pi}E_0(2-\delta_{0,m})\times F_2^{(m)}(\mu,\mu_0)\frac{\tau}{\mu_0}e^{-\tau/\mu_0}$$

II.
$$\mu=0:\int_\tau^T e^{-(t-\tau)/\mu}A(t)\frac{dt}{\mu}\rightarrow\int_0^\infty A(\tau)e^{-s}ds=A(\tau)$$
$$\int_0^\tau e^{-(\tau-t)/\mu}A(t)\frac{dt}{\mu}\rightarrow\int_0^\infty A(\tau)e^{-s}ds=A(\tau)$$

where $A(t)$ is arbitrary.

III. $\mu=0,\ \tau\neq 0,\ \tau\neq T$:
$$I_{1,0}^{(m)}(\tau,0)=\frac{(1-k)}{4\pi}E_0(2-\delta_{0,m})F_1^{(m)}(0,\mu_0)e^{-\tau/\mu_0}$$
$$I_{2,0}^{(m)}(\tau,0)=\frac{(1-k)}{4\pi}E_0(2-\delta_{0,m})F_2^{(m)}(0,\mu_0)e^{-\tau/\mu_0}$$

IV. $\mu=0,\ \tau=0$:
$$I_{1,0}^{(m)}(0,0)=\frac{(1-k)}{4\pi}E_0(2-\delta_{0,m})F_1^{(m)}(0,\mu_0)$$
$$I_{2,0}^{(m)}(0,0)=0$$

V. $\tau=0$ and any μ and μ_0
$$I_{1,0}^{(m)}(0,\mu)\frac{(1-k)}{4\pi}E_0(2-\delta_{0,m})\times\frac{F_1^{(m)}(\mu,\mu_0)\mu_0}{\mu+\mu_0}\left(1-\exp\left[-\frac{\mu+\mu_0}{\mu\mu_0}T\right]\right)$$
$$I_{2,0}^{(m)}(0,\mu)=0$$

VI. $\tau=T$ and any μ
$$I_{1,0}^{(m)}(T,\mu)=0$$

APPENDIX 2

The evaluation of the emission integrals of (10), using the assumption of a piecewise linear distribution of $B(\tau_E)$, results in the distribution of radiative intensities leaving the upper and lower boundaries of each sublayer. Successive application of (25) and employment of the proper boundary conditions, as described in section 3.3, for the m^*th sublayer the upwardly directed intensities $I_1^{(m=0)}(T_E^{(m^*-1)},\mu)$ at its upper boundary, and the downwardly directed intensities $I_2^{(m=0)}(T_E^{(m^*)},\mu)$ at its lower boundary, gives the following relationships:

$$\begin{aligned}I_1^{(m=0)}(T_E^{(m^*-1)},\mu)&=kB_0^{(m^*)}+kB_1^{(m^*)}\mu\\&+\exp[-T_E^{(m^*)}/\mu]\{-kB_0^{(m^*)}-kB_1^{(m^*)}[T_E^{(m^*)}+\mu]\\&+kB_0^{(m^*+1)}\mu+kB_1^{(m^*+1)}\mu\}\\&+\exp[-(T_E^{(m^*)}+T_E^{(m^*+1)})/\mu]\{-kB_0^{(m^*+1)}\\&-kB_1^{(m^*+1)}[T_E^{(m^*+1)}+\mu]+kB_0^{(m^*+2)}+kB_1^{(m^*+2)}\mu\}\\&+\dots+\exp[-(T_E^{(m^*)}+T_E^{(m^*+1)}+\dots+T_E^{(n^*-1)})/\mu]\\&\times\{-kB_0^{(n^*-1)}-kB_1^{(n^*-1)}[T_E^{(n^*-1)}+\mu]\\&+kB_0^{(n^*)}+kB_1^{(n^*)}\mu\}\\&+\exp[-(T_E^{(m^*)}+\dots+T_E^{(n^*-1)}+T_E^{(n^*)})/\mu]\\&\times\{B_G-kB_0^{(n^*)}-kB_1^{(n^*)}[T^{(n^*)}+\mu]\}\end{aligned}$$

The black body radiation B_G is the boundary condition at the lower fog boundary as required by equation (6).

$$\begin{aligned} I_2^{(m-0)}(T_E^{(m^*)},\mu) &= kB_0^{(m^*)} + kB_1^{(m^*)}[T_E^{(m^*)}-\mu] \\ &+ \exp[-T_E^{(m^*)}/\mu]\{-kB_0^{(m^*)}+kB_1^{(m^*)}\mu \\ &+ kB_0^{(m^*-1)} + kB_1^{(m^*-1)}[T_E^{(m^*-1)}-\mu]\} \\ &+ \exp[-(T_E^{(m^*)}+T_E^{(m^*-1)})/\mu]\{-kB_0^{(m^*-1)} \\ &+ kB_1^{(m^*-1)}\mu + kB_0^{(m^*-2)} + kB_1^{(m^*-2)}[T_E^{(m^*-2)}-\mu]\} \\ &+ \dots + \exp[-(T_E^{(m^*)}+T_E^{(m^*-1)}+\dots+T_E^{(2)})/\mu] \\ &\times\{-kB_0^{(2)}+kB_1^{(2)}\mu+kB_0^{(1)}+kB_1^{(1)}[T_E^{(1)}-\mu]\} \\ &+ \exp[-(T_E^{(m^*)}+T_E^{(m^*-1)}+\dots+T_E^{(2)}+T_E^{(1)})/\mu] \\ &\times\{I_2^{(m-0)}T_D,\mu)-kB_0^{(1)}+kB_1^{(1)}\mu\} \end{aligned}$$

The quantity $I_2^{(m-0)}(T_D,\mu)$, as required by equation (6), represents the upper boundary condition of the fog. It is the downward intensity emerging at the lower boundary of the layer D.

APPENDIX 3

The approximation of the phase function (equation 2) requires the knowledge of the expansion coefficients p_l. From previously tabulated values of the phase function, these are computed from

$$p_l = \frac{2l+1}{2}\int_{-1}^{+1} p(\cos\theta)\, P(\cos\theta)\, d\cos\theta$$

This equation can be derived (Baur, 1953[1]) by the method of least squares and by means of the orthogonality properties of the spherical functions as described, for example, by Whitaker & Watson, 1946.

Consider briefly Figs. 6 and 7. The solid line of Fig. 6 ($\lambda = 1.13$ microns) is plotted on the basis of 181 equally incremented scattering angles using the data provided by equation (33). Numerical computations indicate that only very minor additional details of the phase function are revealed by including more scattering angles. The undulating line, approximating the "exact" phase function is obtained on the basis of 158 terms of the Legendre expansion. Each p_l-coefficient incorporates all previously tabulated values of the phase function. The general outline of the phase function is well approximated although some discrepancies exist. These can only be removed by including many more terms in the expansion which makes it impractical for radiative transfer computations.

Fig. 7 ($\lambda = 10$ microns) does not require a very dense tabulation since no fine structure is involved. It is plotted on the basis of 22 non-equally incremented scattering angles. A comparison of the "exact" and approximated phase functions is shown in the following table for randomly selected scattering angles.

[1] Referenced as Linkes Meteorologisches Taschenbuch, 1953.

Comparison table of phase functions for randomly selected scattering angles

Scattering angle	$\lambda = 1.13$ microns			$\lambda = 10.0$ microns	
	$\frac{p}{4\pi}$ (exact)	$\frac{p}{4\pi}$ (approx.)	$\frac{p\text{ (exact)}}{p\text{ (approx.)}}$	$\frac{p}{4\pi}$ (exact)	$\frac{p}{4\pi}$ (approx.)
0°	0.3603×10^2	0.4811×10^2	0.749	1.4300	1.4300
6°	0.2800×10^2	0.3115×10^2	0.899	1.3524	1.3524
18°	0.4186	0.3968	1.055	0.8696	0.8695
40°	0.9588×10^{-1}	0.9875×10^{-1}	0.966	0.1563	0.1562
76°	0.1055×10^{-1}	0.1166×10^{-1}	0.905	0.1155×10^{-1}	0.0155×10^{-1}
112°	0.3887×10^{-2}	0.4550×10^{-2}	0.854	0.3438×10^{-2}	0.3444×10^{-2}
150°	0.1709×10^{-1}	0.1748×10^{-1}	0.978	0.2898×10^{-2}	0.2895×10^{-2}
180°	0.4653×10^{-1}	0.4280×10^{-1}	1.087	0.3627×10^{-2}	0.3658×10^{-2}

The phase function of the infrared wavelength is approximated with very high precision. Indeed, the same is true for the entire infrared spectrum. The phase function of the solar spectrum covers a range of values of four powers of ten which makes a high precision approximation for all scattering angles very difficult. The largest deviation occurs for a scattering angle of zero degrees. A present analysis investigating the effect of deviations from the "exact" scattering function indicates that the transfer calculations are not significantly affected. Results of this new investigation will be publicized shortly.

РАСПРЕДЕЛЕНИЕ РАДИАЦИОННОЙ ЭНЕРГИИ В ПРИЗЕМНОМ ТУМАНЕ

В работе рассматривается распределение солнечной и инфракрасной радиации в многократно рассеивающем и поглощающем тумане, состоящем из водяных капель и водяного пара. Приведено итерационное решение уравнения переноса, сформулированное Чандрасекаром (1960), которое применено для получения интенсивностей радиации, потоков и их вертикального изменения для всего инфракрасного спектра. Достаточное число примеров вычислений выполнено также для солнечного спектра, для проверки применимости числовой процедуры, для всего теплового спектра. Все вычисления приведены для двух моделей туманов, представляющих собой низкий и высокий туман с концентрацией капельной воды в облаках 0,1 *г/м*³. Учитывается точная структура спектральных линий. Результаты вычислений подтверждают применимость метода для всего спектра для тумана, распространяющегося до высоты, по крайней мере, 160 метров. Предполагается, что разработанная процедура вычислений способна дать информацию о радиационном поведении облаков и туманов гораздо более толстых.